nature physics

LETTERS

https://doi.org/10.1038/s41567-020-0942-5

Probing chiral edge dynamics and bulk topology of a synthetic Hall system

Thomas Chalopin[1,3], Tanish Satoor[1,3], Alexandre Evrard[1], Vasiliy Makhalov[1,2], Jean Dalibard[1], Raphael Lopes[1] and Sylvain Nascimbene[1]✉

Quantum Hall systems are characterized by quantization of the Hall conductance—a bulk property rooted in the topological structure of the underlying quantum states[1]. In condensed matter devices, material imperfections hinder a direct connection to simple topological models[2,3]. Artificial systems, such as photonic platforms[4] or cold atomic gases[5], open novel possibilities by enabling specific probes of topology[6–13] or flexible manipulation, for example using synthetic dimensions[14–21]. However, the relevance of topological properties requires the notion of a bulk, which was missing in previous works using synthetic dimensions of limited sizes. Here, we realize a quantum Hall system using ultracold dysprosium atoms in a two-dimensional geometry formed by one spatial dimension and one synthetic dimension encoded in the atomic spin $J=8$. We demonstrate that the large number of magnetic sublevels leads to distinct bulk and edge behaviours. Furthermore, we measure the Hall drift and reconstruct the local Chern marker, an observable that has remained, so far, experimentally inaccessible[22]. In the centre of the synthetic dimension—a bulk of 11 states out of 17—the Chern marker reaches 98(5)% of the quantized value expected for a topological system. Our findings pave the way towards the realization of topological many-body phases.

In two-dimensional (2D) electron gases, quantization of the Hall conductance results from the non-trivial topological structuring of the quantum states of an electron band. For an infinite system, this topological character is described by the Chern number $\mathcal{C}$, a global invariant taking a non-zero integer value that is robust to relatively weak disorder[1]. In a real finite-sized system, the non-trivial topology further leads to in-gap excitations delocalized over the edges, characterized by unidirectional motion exempt from backscattering[3]. Such protected edge modes, together with their generalization to topological insulators, topological superconductors or fractional quantum Hall states[23,24], lie at the heart of possible applications in spintronics[25] or quantum computing[26].

In electronic quantum Hall systems, the topology manifests itself via the spectacular robustness of the Hall conductance quantization to finite-size or disorder effects[27]. Nonetheless, such perturbations typically lead to conducting stripes surrounding insulating domains of localized electrons, making the comparison with simple defect-free models challenging. In topological insulators or fractional quantum Hall systems, topological properties are more fragile, and can only be revealed in very clean samples[23,24]. Recent experiments with topological quantum systems in photonic or atomic platforms[5,28] have created new possibilities, from the realization of emblematic models of topological matter[6,29,30] to the application of well-controlled edge and disorder potentials. In such systems, internal degrees of freedom can be used to simulate a synthetic dimension of finite size with sharp-edge effects[14–21]. Encoding a synthetic dimension in the time domain can also give access to higher-dimensional physics[31,32].

In this work, we engineer a topological system with ultracold bosonic ^{162}Dy atoms based on coherent light-induced couplings between an atom's motion and the electronic spin $J=8$, with relevant dynamics along two dimensions—one spatial dimension and a synthetic dimension encoded in the discrete set of $2J+1=17$ magnetic sublevels. These couplings give rise to an artificial magnetic field, such that our system realizes an analogue of a quantum Hall ribbon. In the lowest band, we characterize the dispersionless bulk modes, where motion is inhibited due to a flattened energy band, and edge states, where the particles are free to move in one direction only. We also study elementary excitations to higher bands, which take the form of cyclotron and skipping orbits. We furthermore measure the Hall drift induced by an external force, and infer the local Hall response of the band via the local Chern marker, which quantifies topological order in real space[22]. Our experiments show that the synthetic dimension is large enough to allow for a meaningful bulk with robust topological properties. Numerical simulations of interacting bosons moreover show that our system can host quantum many-body systems with non-trivial topology, such as mean-field Abrikosov vortex lattices or fractional quantum Hall states.

The atom dynamics is induced by two-photon optical transitions involving counter-propagating laser beams along x (Fig. 1a), and coupling of successive magnetic sublevels m (refs. [33,34]). Here, the integer m ($-J\leq m\leq J$) quantifies the spin projection along the direction z of an external magnetic field. The spin coupling amplitudes then inherit the complex phase Kx of the interference between both lasers, where $K=4\pi/\lambda$ and $\lambda=626.1$ nm is the light wavelength (Fig. 1b). Given the Clebsch–Gordan algebra of atom–light interactions for the dominant optical transition, the atom dynamics is described by the Hamiltonian

$$\hat{H}=\frac{1}{2}M\hat{v}^2-\frac{\hbar\Omega}{2}\left(\mathrm{e}^{-iK\hat{x}}\hat{J}_++\mathrm{e}^{iK\hat{x}}\hat{J}_-\right)+V(\hat{J}_z) \qquad (1)$$

where M is the atom mass, $\hat{v}$ is its velocity and $\hat{J}_z$ and $\hat{J}_\pm$ are the spin projection and ladder operators. The coupling Ω is proportional to both laser electric fields, and the potential $V(\hat{J}_z)=-\hbar\Omega\hat{J}_z^2/(2J+3)$ stems from rank-2 tensor light shifts (see Methods and Supplementary Information).

A light-induced spin transition $m\to m+1$ is accompanied by a momentum kick $-p_{\mathrm{rec}}\equiv-\hbar K$ along x, such that the canonical

[1]Laboratoire Kastler Brossel, Collège de France, CNRS, ENS-PSL University, Sorbonne Université, Paris, France. [2]Present address: ICFO-The Institute of Photonic Sciences, Barcelona, Spain. [3]These authors contributed equally: Thomas Chalopin, Tanish Satoor. ✉e-mail: sylvain.nascimbene@lkb.ens.fr

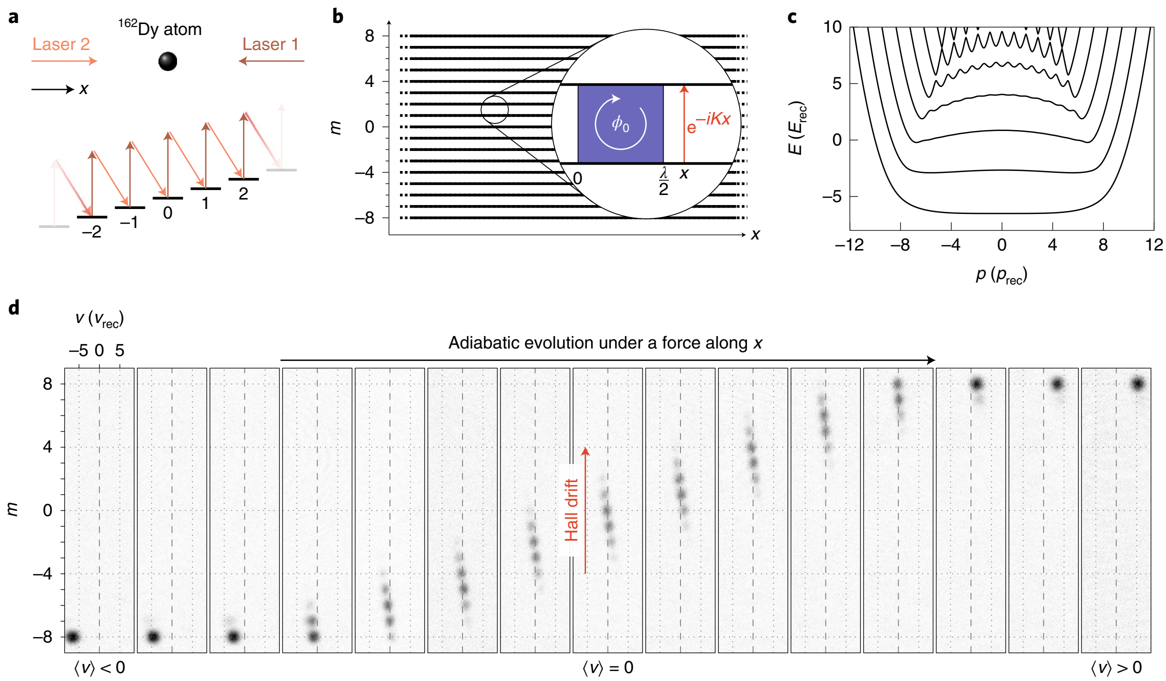

Fig. 1 | Synthetic Hall system. a, Laser configuration used to couple the magnetic sublevels m of a ^{162}Dy atom (with $-J\leq m\leq J$ and $J=8$; only a few m values are represented). **b**, Interpreting the spin projection as a synthetic dimension, the system is mapped to a 2D ribbon of finite width. The photon recoil $p_{\rm rec}=\hbar K$ imparted on a spin transition leads to complex-valued hopping amplitudes along m, equivalent to the Aharonov–Bohm phase of a charged particle evolving in a magnetic field. The blue area represents a magnetic unit cell pierced by one flux quantum ϕ_0. **c**, Dispersion relation describing the quantum level structure for $\hbar\Omega=E_{\rm rec}$, with flattened energy bands reminiscent of Landau levels. **d**, The lowest energy band is explored by applying an external force. We probe the velocity and magnetic projection distributions by imaging the atomic gas after an expansion under a magnetic field gradient. We find three types of behaviour: free motion with negative (positive) velocity on the bottom edge $m=-J$ (top edge $m=J$) and zero average velocity in the bulk. Each panel corresponds to a single-shot image.

momentum $\hat{p}=M\hat{v}+p_{\rm rec}\hat{J}_z$ is a conserved quantity. After a unitary transformation defined by the operator $\hat{U}=\exp(iK\hat{x}\hat{J}_z)$, the Hamiltonian (1) can be rewritten, for a given momentum p, as

$$\hat{H}_p=\frac{(p-p_{\rm rec}\hat{J}_z)^2}{2M}-\hbar\Omega\hat{J}_x+V(\hat{J}_z)\tag{2}$$

We can make an analogy between this Hamiltonian and the ideal Landau one, given by

$$\hat{H}_{\rm Landau}=\frac{(\hat{p}_x-eB\hat{y}^2)}{2M}+\frac{\hat{p}_y^2}{2M}\tag{3}$$

which describes the dynamics of an electron of charge $-e$ evolving in the x–y plane under a perpendicular magnetic field B. The analogy between the two systems can be made upon the identifications $\hat{J}_z\leftrightarrow\hat{y}$ and $p_{\rm rec}\leftrightarrow eB$. The term $\hat{J}_x$ in equation (2) plays the role of the kinetic energy along the synthetic dimension, because it couples neighbouring m levels with real positive coefficients, similarly to the discrete form of the Laplacian operator $\propto\hat{p}_y^2$ in equation (3) (see Supplementary Information). The range of magnetic projections being limited, our system maps onto a Hall system in a ribbon geometry bounded by the edge states $m=\pm J$. The relevance of the analogy is confirmed by the structure of energy bands $E_n(p)$ expected for the Hamiltonian (2) describing our system, shown in Fig. 1c. The energy dispersion of the first few bands is strongly reduced for $|p|\lesssim Jp_{\rm rec}$, reminiscent of dispersionless Landau levels. A parabolic dispersion is recovered for $|p|\gtrsim Jp_{\rm rec}$, similar to the ballistic edge modes of a quantum Hall ribbon[3]. The flatness of the lowest energy band, for $\hbar\Omega\approx E_{\rm rec}$, results from the compensation of two dispersive effects, namely the variation of $\hat{J}_x$ matrix elements and the extra term, $V(\hat{J}_z)$ (see Supplementary Information).

We first characterize the ground band using quantum states of arbitrary values of momentum p. We begin with an atomic gas spin-polarized in $m=-J$, and with a negative mean velocity $\langle\hat{v}\rangle=-6.5(1)v_{\rm rec}$ (with $v_{\rm rec}\equiv p_{\rm rec}/M$), such that it corresponds to the ground state of equation (2) with $p=-14.5(1)p_{\rm rec}$. The gas temperature $T=0.55(6)\,\mu$K is such that the thermal velocity broadening is smaller than the recoil velocity $v_{\rm rec}$. We then slowly increase the light intensity up to a coupling $\hbar\Omega=1.02(6)E_{\rm rec}$, where $E_{\rm rec}\equiv p_{\rm rec}^2/(2M)$ is the natural energy scale in our system. Subsequently, we apply a weak force F_x along x, such that the state adiabatically evolves in the ground energy band with $\dot{p}=F_x$, until the desired momentum is reached (see Methods). We measure the distribution of velocity v and spin projection m by imaging the atomic gas after a free flight in the presence of a magnetic field gradient.

The main features of Landau level physics are visible in the raw images shown in Fig. 1d. Depending on the momentum p, the system exhibits three types of behaviour. (1) When spin-polarized in $m=-J$, the atoms move with a negative mean velocity $\langle\hat{v}\rangle$, consistent with a left-moving edge mode. (2) When the velocity approaches zero under the action of the force F_x, the system experiences a series of resonant transitions to higher m sublevels—in other words a transverse Hall drift along the synthetic dimension. In this regime the atom's motion is inhibited along x, as expected for a quasi non-dispersive band. (3) Once the edge $m=J$ is reached, the velocity $\langle\hat{v}\rangle$ rises again, corresponding to a right-moving edge mode. Overall, while exploring the entire ground band under the action of a force along x, the atoms are pumped from one edge to the other along the synthetic dimension.

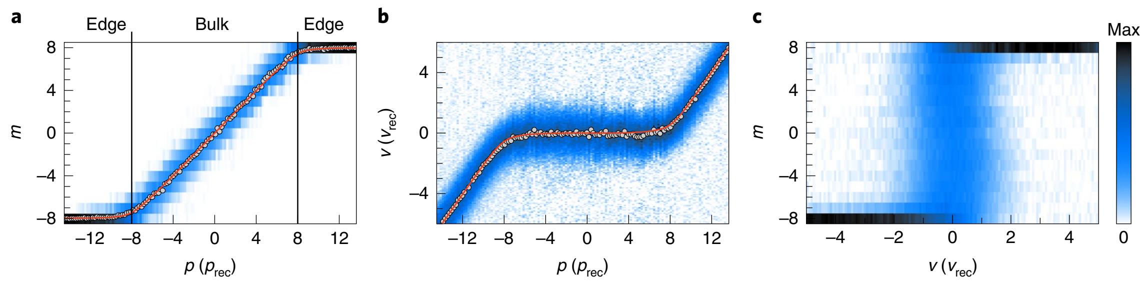

Fig. 2 | Ground band characterization. a, Spin projection distribution Π_m as a function of momentum p, with the mean spin projection $\langle\hat{J}_z\rangle$ (grey dots) and the theoretical prediction $(p-M\partial_pE_0)/p_{\rm rec}$ (red line). **b**, Velocity distribution, together with the mean velocity $\langle\hat{v}\rangle$ (grey dots) and the expected value, given by the derivative of the band dispersion ∂_pE_0 (red line). **c**, Local density of states obtained by integrating the measured distributions in (v, m) space over all momenta. All error bars are the $1-\sigma$ s.d. of typically five measurement repetitions.

To distinguish between bulk and edge modes, Fig. 2a shows the spin projection probabilities Π_m as a function of momentum p. We find that the edge probabilities $\Pi_{m=\pm J}$ exceed 1/2 for $|p|>8.0(1)p_{\rm rec}$, defining the edge mode sectors—with the bulk modes in between. We study the system dynamics via its velocity distribution and mean velocity $\langle\hat{v}\rangle$, shown in Fig. 2b. We observe that the velocity of bulk modes remains close to zero, which shows via the Hellmann–Feynman relation $\langle\hat{v}\rangle=\partial E_0/\partial p$ that the ground band is almost flat.

The measured residual mean velocities allow us to infer a dispersion $\Delta E_0^{\text{pk-pk}}=1.2(5)\ E_{\rm rec}$ in the bulk mode region—nearly 2% of the free-particle dispersion expected over the same range of momenta. By contrast, edge modes are characterized by a velocity $\langle\hat{v}\rangle\simeq(p-p_0)/M$, corresponding to ballistic motion, albeit with the restriction $\langle\hat{v}\rangle<0$ for edge modes close to $m=-J$ and $\langle\hat{v}\rangle>0$ at the opposite edge. We also characterize correlations between velocity v and spin projection m over the full band, via the local density of states (LDOS) in (v, m) space, integrated over p. We stress here that the LDOS only involves gauge-independent quantities and could thus be generalized to more complex geometries lacking translational invariance. As shown in Fig. 2c, it also reveals characteristic quantum Hall behaviour, namely inhibited dynamics in the bulk and chiral motion on the edges.

The ideal Landau level structure of a charged particle evolving in two dimensions in a transverse magnetic field is characterized by a harmonic energy spacing $\hbar\omega_c$, set by the cyclotron frequency $\omega_c=eB/M$. We test this behaviour in our system by studying elementary excitations above the ground band, via the trajectories of the centre of mass following a velocity kick $v_{\rm kick}\simeq v_{\rm rec}$. To access the real-space position of the atoms, we numerically integrate their centre-of-mass velocity evolution (see Methods). As shown in Fig. 3 (blue dots), we measure almost closed trajectories in the bulk, consistent with the periodic cyclotron orbits expected for an infinite Hall system. We checked that this behaviour remains valid for larger excitation strengths, until one couples to highly dispersive excited bands (for velocity kicks $v_{\rm kick}\gtrsim 2v_{\rm rec}$, see Methods). Close to the edges, the atoms experience an additional drift and their trajectories are similar to classical skipping orbits bouncing on a hard wall. In particular, the drift orientation only depends on the considered edge, irrespective of the kick direction. We report in the inset of Fig. 3 the frequencies of velocity oscillations, which agree well with the expected cyclotron gap to the first excited band. We find that the gap is almost uniform within the bulk mode sector, with a residual variation in the range $\omega_c=3.0(1)$–$3.8(1)E_{\rm rec}/\hbar$.

We now investigate the key feature of Landau levels, namely their quantized Hall response, which is intrinsically related to their topological nature. In a ribbon geometry, the Hall response of a particle corresponds to the transverse velocity acquired upon applying a potential difference across the edges (Fig. 4a). In our system,

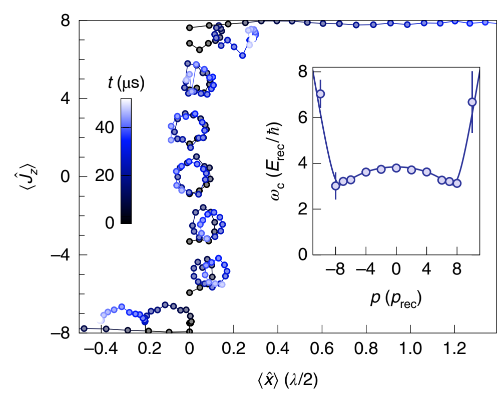

Fig. 3 | Cyclotron and skipping orbits. Trajectories in (x, m) space following a velocity kick $v_{\rm kick}\simeq v_{\rm rec}$, starting at $\langle\hat{x}\rangle=0$, and for different initial momentum states (blue dots). The colour encodes the time evolution. Inset: frequencies extracted from the velocity dynamics (blue dots) and compared with the expected cyclotron gap for $\hbar\Omega=E_{\rm rec}$ (blue line). Error bars show the $1-\sigma$ statistical uncertainty calculated from a bootstrap sampling analysis performed on more than 100 pictures.

such a potential corresponds to a Zeeman term $-F_m\hat{J}_z$ added to Hamiltonian (2), which can now be recast as

$$\hat{H}_p-F_m\hat{J}_z=\hat{H}_{p+Mv'}-v'p\quad\text{with}\quad v'=F_m/p_{\rm rec}$$

such that the force acts as a momentum shift Mv' in the reference frame with velocity v'. In the weak force limit, the perturbed state remains in the ground band, and its mean velocity reads

$$\langle\hat{v}\rangle=\langle\hat{v}\rangle_{F_m=0}-\mu F_m,\quad\text{where}\quad\mu=\frac{1}{p_{\rm rec}}\frac{\partial}{\partial p}(p-M\langle\hat{v}\rangle)$$

is the Hall mobility. This expression shows that the Hall response to a weak force can be related to the variation of the mean velocity within the ground band, which we show in Fig. 2b. In practice, the velocity derivative at momentum p is evaluated using momentum states in the domain $(p-p_{\rm rec}, p+p_{\rm rec})$, corresponding to an evaluation of the Hall drift under a force $-2E_{\rm rec}/\ell<F_m<2E_{\rm rec}/\ell$, where $\ell=1$ is the unit length along the synthetic dimension. We present in Fig. 4b the Hall mobility $\mu(p)$ deduced from this procedure. For bulk modes, it remains close to the value $\mu=1/p_{\rm rec}$, which corresponds to the classical mobility $\mu=1/(eB)$ in the equivalent Hall system. The mobility decreases in the edge mode sector, as expected

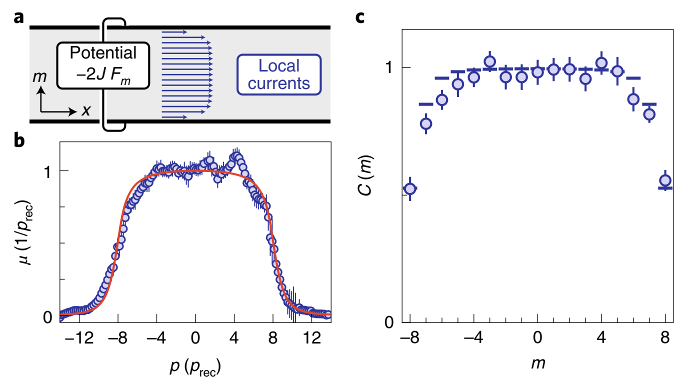

Fig. 4 | The Hall response. a, The Hall response is determined from the measurement of local currents in the real dimension that result from the application, in synthetic space, of a potential difference $-2JF_m$ between the edges. **b**, Hall mobility $\mu(p)$ measured for states of momenta p via their increase of velocity on application of a small force F_m along m. **c**, Local Chern marker as a function of m, corresponding to the integrated mobility $\mu(p)$ weighted by the projection probability $\Pi_m(p)$. Error bars represent the $1-\sigma$ statistical uncertainty calculated from a bootstrap sampling analysis over typically 100 pictures (**b**) and 1,000 pictures (**c**).

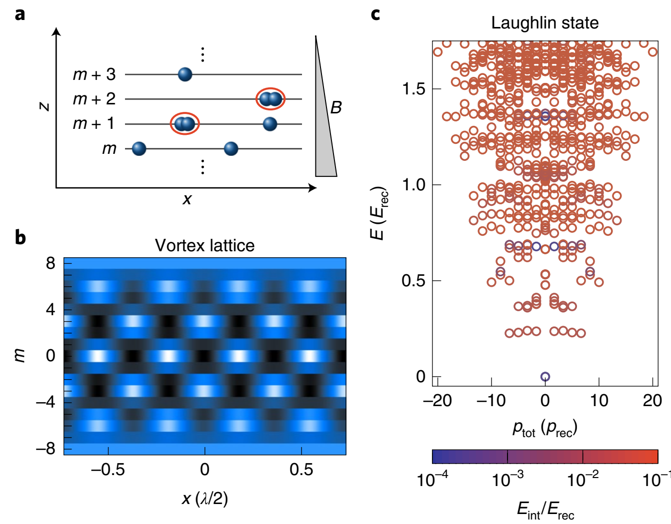

Fig. 5 | Simulations of topological many-body systems. a, Proposed scheme to engineer contact interactions along both directions x and m. A magnetic field gradient spatially separates the different m states along z, such that collisions (represented by the red ellipses) only occur for atoms in the same magnetic sublevel m. **b**, Density distribution of a Bose–Einstein condensate, with a chemical potential at ~$2E_{rec}$ above the single-particle ground-state energy. **c**, Many-body spectrum of a system of $N=5$ interacting atoms, where the colour encodes the interaction energy. We use periodic boundary conditions along x, with a circumference $L=0.6(\lambda/2)$ allowing for $N_{orb}=9$ orbitals at low energy, compatible with the Laughlin state. The residual energy dispersion between these orbitals is minimized by using a coupling strength $\Omega=0.5E_{rec}/\hbar$.

for topologically protected boundary states whose ballistic motion is undisturbed by the magnetic field.

We use the measured drift of individual quantum states to infer the overall Hall response of the ground band. As for any spatially limited sample, our system does not exhibit a gap in the energy spectrum due to the edge mode dispersion. In particular, high-energy edge modes of the ground band are expected to resonantly hybridize with excited bands upon disorder, such that defining the Hall response of the entire ground band is not physically meaningful. We thus only consider the energy branch $E<E^*$, where E^* lies in the middle of the first gap at zero momentum (see Methods). We characterize the (inhomogeneous) Hall response of this branch via the local Chern marker

$$C(m) \equiv 2\pi \mathrm{Im}\langle m|[\hat{P}\hat{x}\hat{P}, \hat{P}\hat{J}_z\hat{P}]|m\rangle = \int_{E(p)<E^*} \mathrm{d}p\, \Pi_m(p)\mu(p)$$

where $\hat{P}$ projects on the chosen branch[22,35]. This local geometrical marker quantifies the adiabatic transverse response in position space and matches the integer Chern number $\mathcal{C}$ in the bulk of a large, defect-free system. Here, it is given by the integrated mobility $\mu(p)$, weighted by the spin projection probability $\Pi_m(p)$ (see Methods). As shown in Fig. 4c, we identify a plateau in the range $-5\le m\le 5$. There, the average value of the Chern marker, $\overline{C}=0.98(5)$, is consistent with the integer value $\mathcal{C}=1$, the Chern number of an infinite Landau level. This measurement shows that our system is large enough to reproduce a topological Hall response in its bulk. For positions $|m|\ge 6$, we measure a decrease of the Chern marker, which we attribute to non-negligible correlations with the edges.

Such a topological bulk is a prerequisite for the realization of emblematic phases of 2D quantum Hall systems, as we now confirm via numerical simulations of interacting quantum many-body systems. In our system, collisions between atoms a priori occur when they are located at the same position x, irrespective of their spin projections m, m', leading to highly anisotropic interactions. Although this feature leads to an interesting phenomenology[36], we propose to control the interaction range by spatially separating the different m states using a magnetic field gradient, suppressing both contact and dipole–dipole interactions for $m\neq m'$, as illustrated in Fig. 5a (see Methods and Supplementary Information). The system then becomes truly 2D and closely related to the seminal work of ref. [33], albeit with a discrete spatial dimension with sharp walls. In the following, we discuss the many-body phases expected for bosonic atoms with such short-range interactions, assuming, for simplicity, repulsive interactions of equal strength for each projection m.

We first consider the case of a large filling fraction $\nu\equiv N_{at}/N_\phi\gg 1$, where N_ϕ is the number of magnetic flux quanta in the area occupied by N_{at} atoms, as realized in previous experiments on rapidly rotating gases[37,38]. In this regime and at low temperature, the system forms a Bose–Einstein condensate that spontaneously breaks translational symmetry, leading to a triangular Abrikosov lattice of quantum vortices (Fig. 5b). Owing to the hard-wall boundary along m, one expects phase transitions between vortex lattice configurations when tuning the coupling strength Ω and the chemical potential, similar to the phenomenology of type-II superconductors in confined geometries[39] (see Methods).

For lower filling fractions $\nu\approx 1$, one expects strongly correlated ground states analogous to fractional quantum Hall states[40]. We present in Fig. 5c a numerical calculation of the many-body spectrum for $N_{at}=5$ atoms with periodic boundary conditions along x, corresponding to a cylinder geometry. We choose the circumference such that the number of orbitals $N_{orb}=9$ in the bulk region of the lowest band matches the number $N_{orb}=2N_{at}-1$ required to construct the Laughlin wavefunction. For contact interactions parametrized by a Haldane pseudopotential of amplitude $U=E_{rec}$, we numerically find a ground state separated by an energy gap $E_{gap}\simeq 0.23E_{rec}=k_B\times 140\,\mathrm{nK}$ from the rest of the excitations. It also exhibits a very small interaction energy E_{int}, indicating anti-bunching between atoms, which is a hallmark of the Laughlin state.

The realization of a quantum-Hall system based on a large synthetic dimension, as discussed here, is a promising setting for future realizations of topological quantum matter. An important asset of our set-up is the large cyclotron energy, measured in the range $\hbar\omega_c \simeq k_B \times 1.8-2.3\,\mu K$, much larger than the typical temperatures of quantum degenerate gases, thus enabling the realization of strongly correlated states at realistic temperatures. The techniques developed here could give access to complex correlation effects, such as flux attachment via cyclotron orbits[41] or charge fractionalization via adiabatic pumping[42] or the centre-of-mass Hall response[43]. Our protocol could also be extended to fermionic isotopes of dysprosium, with a synthetic dimension given by the hyperfine spin of the lowest energy state, $F=21/2$ for ^{161}Dy, leading to an even larger bulk. At low temperature and unit filling of the ground band, the Fermi sea would exhibit an almost quantized Hall response akin to the integer quantum Hall effect.

Online content

Any methods, additional references, Nature Research reporting summaries, source data, extended data, supplementary information, acknowledgements, peer review information; details of author contributions and competing interests; and statements of data and code availability are available at https://doi.org/10.1038/s41567-020-0942-5.

Received: 13 December 2019; Accepted: 20 May 2020;
Published online: 22 June 2020

References

1. Thouless, D. J., Kohmoto, M., Nightingale, M. P. & denNijs, M. Quantized Hall conductance in a two-dimensional periodic potential. *Phys. Rev. Lett.* **49**, 405–408 (1982).
2. Laughlin, R. B. Quantized Hall conductivity in two dimensions. *Phys. Rev. B* **23**, 5632–5633 (1981).
3. Halperin, B. I. Quantized Hall conductance, current-carrying edge states, and the existence of extended states in a two-dimensional disordered potential. *Phys. Rev. B* **25**, 2185–2190 (1982).
4. Ozawa, T. et al. Topological photonics. *Rev. Mod. Phys.* **91**, 015006 (2019).
5. Goldman, N., Budich, J. C. & Zoller, P. Topological quantum matter with ultracold gases in optical lattices. *Nat. Phys.* **12**, 639–645 (2016).
6. Jotzu, G. et al. Experimental realization of the topological Haldane model with ultracold fermions. *Nature* **515**, 237–240 (2014).
7. Aidelsburger, M. et al. Measuring the Chern number of Hofstadter bands with ultracold bosonic atoms. *Nat. Phys.* **11**, 162–166 (2015).
8. Hu, W. et al. Measurement of a topological edge invariant in a microwave network. *Phys. Rev. X* **5**, 011012 (2015).
9. Mittal, S., Ganeshan, S., Fan, J., Vaezi, A. & Hafezi, M. Measurement of topological invariants in a 2D photonic system. *Nat. Photon.* **10**, 180–183 (2016).
10. Wu, Z. et al. Realization of two-dimensional spin–orbit coupling for Bose–Einstein condensates. *Science* **354**, 83–88 (2016).
11. Fläschner, N. et al. Experimental reconstruction of the Berry curvature in a Floquet Bloch band. *Science* **352**, 1091–1094 (2016).
12. Ravets, S. et al. Polaron polaritons in the integer and fractional quantum Hall regimes. *Phys. Rev. Lett.* **120**, 057401 (2018).
13. Schine, N., Chalupnik, M., Can, T., Gromov, A. & Simon, J. Electromagnetic and gravitational responses of photonic Landau levels. *Nature* **565**, 173–179 (2019).
14. Celi, A. et al. Synthetic gauge fields in synthetic dimensions. *Phys. Rev. Lett.* **112**, 043001 (2014).
15. Mancini, M. et al. Observation of chiral edge states with neutral fermions in synthetic Hall ribbons. *Science* **349**, 1510–1513 (2015).
16. Stuhl, B. K., Lu, H.-I., Aycock, L. M., Genkina, D. & Spielman, I. B. Visualizing edge states with an atomic Bose gas in the quantum Hall regime. *Science* **349**, 1514–1518 (2015).
17. Livi, L. F. et al. Synthetic dimensions and spin–orbit coupling with an optical clock transition. *Phys. Rev. Lett.* **117**, 220401 (2016).
18. Kolkowitz, S. et al. Spin–orbit-coupled fermions in an optical lattice clock. *Nature* **542**, 66–70 (2017).
19. An, F. A., Meier, E. J. & Gadway, B. Direct observation of chiral currents and magnetic reflection in atomic flux lattices. *Sci. Adv.* **3**, e1602685 (2017).
20. Lustig, E. et al. Photonic topological insulator in synthetic dimensions. *Nature* **567**, 356–360 (2019).
21. Ozawa, T. et al. Topological photonics. *Rev. Mod. Phys.* **91**, 015006 (2019).
22. Bianco, R. & Resta, R. Mapping topological order in coordinate space. *Phys. Rev. B* **84**, 241106 (2011).
23. Stormer, H. L., Tsui, D. C. & Gossard, A. C. The fractional quantum Hall effect. *Rev. Mod. Phys.* **71**, S298–S305 (1999).
24. Hasan, M. Z. & Kane, C. L. Colloquium: topological insulators. *Rev. Mod. Phys.* **82**, 3045–3067 (2010).
25. Pesin, D. & MacDonald, A. H. Spintronics and pseudospintronics in graphene and topological insulators. *Nat. Mater.* **11**, 409–416 (2012).
26. Kitaev, A. Y. Fault-tolerant quantum computation by anyons. *Ann. Phys.* **303**, 2–30 (2003).
27. Klitzing, K. V., Dorda, G. & Pepper, M. New method for high-accuracy determination of the fine-structure constant based on quantized Hall resistance. *Phys. Rev. Lett.* **45**, 494–497 (1980).
28. Lu, L., Joannopoulos, J. D. & Soljačić, M. Topological photonics. *Nat. Photon.* **8**, 821–829 (2014).
29. Aidelsburger, M. et al. Realization of the Hofstadter Hamiltonian with ultracold atoms in optical lattices. *Phys. Rev. Lett.* **111**, 185301 (2013).
30. Miyake, H., Siviloglou, G. A., Kennedy, C. J., Burton, W. C. & Ketterle, W. Realizing the Harper Hamiltonian with laser-assisted tunneling in optical lattices. *Phys. Rev. Lett.* **111**, 185302 (2013).
31. Lohse, M., Schweizer, C., Price, H. M., Zilberberg, O. & Bloch, I. Exploring 4D quantum Hall physics with a 2D topological charge pump. *Nature* **553**, 55–58 (2018).
32. Zilberberg, O. et al. Photonic topological boundary pumping as a probe of 4D quantum Hall physics. *Nature* **553**, 59–62 (2018).
33. Lin, Y.-J., Jiménez-García, K. & Spielman, I. B. Spin–orbit-coupled Bose–Einstein condensates. *Nature* **471**, 83–86 (2011).
34. Cui, X., Lian, B., Ho, T.-L., Lev, B. L. & Zhai, H. Synthetic gauge field with highly magnetic lanthanide atoms. *Phys. Rev. A* **88**, 011601 (2013).
35. Kitaev, A. Anyons in an exactly solved model and beyond. *Ann. Phys.* **321**, 2–111 (2006).
36. Barbarino, S., Taddia, L., Rossini, D., Mazza, L. & Fazio, R. Magnetic crystals and helical liquids in alkaline-earth fermionic gases. *Nat. Commun.* **6**, 8134 (2015).
37. Schweikhard, V., Coddington, I., Engels, P., Mogendorff, V. P. & Cornell, E. A. Rapidly rotating Bose–Einstein condensates in and near the lowest Landau level. *Phys. Rev. Lett.* **92**, 040404 (2004).
38. Bretin, V., Stock, S., Seurin, Y. & Dalibard, J. Fast rotation of a Bose–Einstein condensate. *Phys. Rev. Lett.* **92**, 050403 (2004).
39. Abrikosov, A. A. On the magnetic properties of superconductors of the second group. *Sov. Phys. JETP* **5**, 1174–1182 (1957).
40. Kane, C. L., Mukhopadhyay, R. & Lubensky, T. C. Fractional quantum Hall effect in an array of quantum wires. *Phys. Rev. Lett.* **88**, 036401 (2002).
41. Goldman, V. J., Su, B. & Jain, J. K. Detection of composite fermions by magnetic focusing. *Phys. Rev. Lett.* **72**, 2065–2068 (1994).
42. Zeng, T.-S., Wang, C. & Zhai, H. Charge pumping of interacting fermion atoms in the synthetic dimension. *Phys. Rev. Lett.* **115**, 095302 (2015).
43. Taddia, L. et al. Topological fractional pumping with alkaline-earth-like atoms in synthetic lattices. *Phys. Rev. Lett.* **118**, 230402 (2017).

Methods

Details on the experimental protocol. Our experiments began by preparing an ultracold gas of $8(2)\times10^4$ ^{162}Dy atoms at a temperature $T=0.55(6)\,\mu$K, which was then held in an almost symmetrical optical dipole trap with frequency $\bar{\omega}=2\pi\times150\,$Hz, leading to a peak density of $n_0\approx10^{13}\,\mathrm{cm}^{-3}$. The atoms were placed in a magnetic field $B=172(2)\,$mG along the z axis, corresponding to a Zeeman splitting of frequency $\omega_Z=2\pi\times298(3)\,$kHz, with the electronic spin polarized in the absolute ground state $m=-J$. We then turned off the trap and turned on the two laser beams shown in Fig. 1, which differed in frequency by $\omega_{12}=\omega_1-\omega_2$. When ω_{12} was close to the Zeeman splitting ω_Z, a spin transition $m\rightarrow m+1$ occurred via the absorption of one photon from beam 1 and the stimulated emission of one photon in beam 2. In such processes and in the absence of additional external forces, the canonical momentum $\hat{p}=M\hat{v}+\hbar K\hat{J}_z$ is conserved.

The laser beam frequencies were set close to the optical transition at 626.1 nm, which couples the electronic ground state $J=8$ to an excited level $J'=9$. The beams were detuned by $\Delta=2\pi\times22\,$GHz with respect to resonance and were linearly polarized along orthogonal directions, each being at 45° with respect to the z axis. The algebra of the Clebsch–Gordan coefficients of $J\rightarrow J'=J+1$ transitions led to Hamiltonian (2) at resonance ($\omega_{12}=\omega_Z$), with

$$\Omega=\frac{2J+3}{4(J+1)(2J+1)}V_0,\quad V_0=\frac{3\pi c^2\Gamma}{2\omega_0^3}\frac{\sqrt{I_1I_2}}{\Delta}$$

where $I_{1,2}$ are the laser intensities on the atoms, $\Gamma\simeq2\pi\times135\,$kHz is the transition linewidth and ω_0 is its resonant frequency. The value of the coupling Ω was calibrated using an independent method and remained constant over the experimental sequence because the waists of both laser beams were much larger than the region of atomic motion. The Larmor frequency ω_Z was calibrated from the resonance of the Raman transition between $m=-8$ and $m=-7$.

The non-resonant case ($\omega_{12}\neq\omega_Z$) can be reduced to the resonant case in a reference frame moving at a velocity $v_{\mathrm{frame}}=(\omega_Z-\omega_{12})/K$. Note that the required change of frame means that fluctuations of ω_Z contribute to the uncertainties of the measured velocities. We first slowly increased the intensity up to a coupling $\hbar\Omega=1.02(6)E_{\mathrm{rec}}$, where $E_{\mathrm{rec}}\equiv p_{\mathrm{rec}}^2/(2M)$, and then applied an external force F_x on the system via the inertial force resulting from a time-dependent frequency difference, with $F_x=(M/K)\partial_t\omega_{12}$. The preparation of a state in the lowest band with a given momentum p was performed by adiabatically ramping the frequency difference to a final value

$$\omega_{12}=\omega_Z+2\left(\frac{p}{p_{\mathrm{rec}}}+J\right)\frac{E_{\mathrm{rec}}}{\hbar}\qquad(4)$$

We used the relation (4) to define, from the final frequency difference ω_{12}, the quasi-momentum p parametrizing the experimental data. We used a constant ramp rate $\partial_t\omega_{12}\simeq0.22\,\omega_{\mathrm{c,min}}^2$, where $\omega_{\mathrm{c,min}}\simeq3.06\,E_{\mathrm{rec}}/\hbar$ is the minimum cyclotron frequency separating the two lowest energy bands for $\Omega=E_{\mathrm{rec}}/\hbar$. Depending on the target p state, the preparation took between 150 μs and 550 μs. Shot-to-shot fluctuations of the ambient magnetic field induce fluctuations of the Zeeman frequency splitting, hence an error in the value of the prepared momentum p. As shown in Extended Data Fig. 1, the measured error in momentum remains small compared to the recoil momentum p_{rec}, and its root mean square (r.m.s.) deviation $\Delta p\simeq0.06p_{\mathrm{rec}}$ is compatible with the magnetic field fluctuations $\sigma_B=0.7\,$mG measured independently.

We numerically checked the adiabaticity of the state preparation protocol. While preparing $m=+J$, which requires crossing all momentum states, the squared overlap with the ground band remains greater than 0.96 and the deviation of the mean spin projection $\langle\hat{J}_z\rangle$ from the corresponding ground state value is always less than 0.08. The largest deviations occur near $m\simeq\pm7$, where the energy gap to the first excited band is the smallest. This behaviour is consistent with our measurements, showing that the adiabatic transfer to $m=J$ after exploring the entire band is above 97%.

At the end of the experiment, we probed the velocity and spin projection distributions. For this, we abruptly switched off the Raman lasers and subsequently ramped up an inhomogeneous magnetic field that split the different magnetic sublevels along z. After a 4-ms expansion, we took a resonant absorption picture. The measured atom density was split along z according to the magnetic projection m, and the density along x corresponds to the distribution of velocity v ($\omega t_{\mathrm{tof}}\approx4$). Our imaging set-up was such that the 17 magnetic sublevels had different cross-sections. We calibrated the relative cross-sections such that the calculated atom number remained constant for all momentum states, irrespective of their spin composition.

Cyclotron orbits. To probe the excitations of the system we performed a velocity quench, which couples the lowest Landau level to the next higher energy band. The system then responds periodically with a frequency set by the energy difference between the two bands, which for the case of an ideal Hall system would correspond to the cyclotron frequency ω_c. Experimentally, we performed the velocity kick by quenching the detuning ω_{12}, which in practice settles to a steady value after 4 μs. We show in Extended Data Fig. 2a,b an example of coherent oscillations of both magnetization and velocity. We computed the response of the system in real space, x, via a numerical integration of the velocity evolution as shown in Extended Data Fig. 2c. The uncertainty on the Larmor frequency leads to a systematic error on the velocity on the order of $0.1v_{\mathrm{rec}}$, consistent with the small drift of some cyclotron orbits in the bulk.

The response of the system was probed after a velocity kick $v_{\mathrm{kick}}\approx v_{\mathrm{rec}}$. This kick ensures a negligible overlap with the second excited band (smaller than 4%). Although, in an ideal Hall system, all bulk excitations evolve periodically at the cyclotron frequency $\omega_c=qB/M$ due to the harmonic spacing of successive Landau levels, this is not exactly the case in our system. We tested this behaviour by varying the strength of the excitation, which relates to the magnitude of the velocity kick. As shown in Extended Data Fig. 2d, we find that the trajectories cease to be closed and start to drift along the kick direction as the excitation strength exceeds $1.5v_{\mathrm{rec}}$ (Extended Data Fig. 2f). This regime corresponds to the onset of a significant population of higher energy bands $n\geq2$, which illustrates the non-harmonic spectrum of our system.

It is important to note that the excitation protocol described so far is inefficient for large values of p, where the energy gap is much larger. In that regime, a quench of the coupling amplitude Ω leads to a more efficient overlap with higher energy bands. This is shown in Extended Data Fig. 2e, for the case of a sudden branching of the coupling strength to $\hbar\Omega=E_{\mathrm{rec}}$. The system initially at $p=-Jp_{\mathrm{rec}}$ is then effectively coupled to higher energy bands and the bouncing on the hard wall characteristic of classical skipping orbits is clearly visible.

Transverse drift in a Hall system. Our system is analogous to a Hall system in a ribbon geometry (see Supplementary Information for a discussion in the case of a disk geometry). To understand the role of a sharp edge on the physical quantities measured in the main text, we consider an electronic Hall system in a semi-infinite geometry, described by the Landau Hamiltonian (3), written as

$$\hat{H}=\frac{\hat{p}_y^2}{2M}+\frac{1}{2}M\omega_c^2(\hat{y}-\hat{p}_x\ell^2/\hbar)^2$$

with a hard-wall restricting motion to the half-plane $y>0$. Here, we introduce the cyclotron frequency $\omega_c=eB/M$ and the magnetic length $\ell=\sqrt{\hbar/eB}$, assuming a magnetic field B along z.

We first consider semiclassical trajectories in the absence of external forces, which are either closed cyclotron orbits or skipping orbits bouncing on the edge, parametrized by the rebound angle θ (Extended Data Fig. 3a). Applying a perturbative force F along y leads to a drift of cyclotron orbits of velocity $v_d=-F/eB$ along x, corresponding to a Hall mobility $\mu=1/eB$. For skipping orbits, the Hall drift can be expressed analytically as

$$\mu=\frac{1}{eB}\left[1-\left(\frac{\sin\theta}{\theta}\right)^2\right]\qquad(5)$$

The factor of reduction compared to cyclotron orbits, plotted in Extended Data Fig. 3a, smoothly interpolates between 1 for almost closed orbits ($\theta\rightarrow\pi$) and 0 for almost straight orbits ($\theta\rightarrow0$). This behaviour provides a simple explanation of the reduced Hall mobility of edge modes (Fig. 4b).

We extend this reasoning to the quantum dynamics in the lowest energy band. In a semi-infinite geometry, the eigenstates of Hamiltonian (5) can be indexed by the momentum p along x, and are expressed as[44]

$$\begin{aligned}\psi_p(x,y)&=\frac{e^{ipx/\hbar}}{\sqrt{2\pi\hbar}}\phi_p(y)\\ \phi_p(y)&\propto D_{\epsilon(p)-1/2}\left[\sqrt{2}(y-p\ell^2/\hbar)/\ell\right]\end{aligned}\qquad(6)$$

where $D_\nu(z)$ is the parabolic cylinder function and $\epsilon(p)=E_0(p)/\hbar\omega_c$ is the reduced energy determined by the boundary condition $D_{\epsilon(p)-1/2}(-\sqrt{2}p\ell/\hbar)=0$ (Extended Data Fig. 3b). By summing over all momentum states of the ground band, we compute the local density of state in (v_x, y) coordinates plotted in Extended Data Fig. 3d. Far from the edge $y\gg\ell$, the velocity distribution is a Gaussian centred on $v_x=0$, of r.m.s. width $\delta v_x=\hbar/(M\ell)$. The distribution is shifted to negative velocities when approaching the edge $y=0$, as expected for chiral edge modes.

We now consider the Hall response of the system by studying the perturbative action of a force F along y, described by the Hamiltonian

$$\begin{aligned}\hat{H}_p'&=\frac{\hat{p}_y^2}{2M}+\frac{1}{2}M\omega_c^2(\hat{y}-p\ell^2/\hbar)^2-F\hat{y}\\ &=\frac{\hat{p}_y^2}{2M}+\frac{1}{2}M\omega_c^2\left(\hat{y}-\frac{p\ell^2}{\hbar}-\frac{F}{M\omega_c^2}\right)^2+\mathcal{E}(p)\\ \mathcal{E}(p)&=-\frac{pF}{M\omega_c}-\frac{F^2}{2M\omega_c^2}\end{aligned}$$

We identify the perturbed Hamiltonian $\hat{H}_p'$ as $\hat{H}_{p+F/\omega_c}$, with an additional energy shift $\mathcal{E}(p)$. Assuming the system to remain in the ground band, the group velocity of a localized wavepacket becomes

$$\langle\hat{v}\rangle'=v_0(p+F/\omega_c)-\frac{F}{M\omega_c},\quad v_0(p)=\frac{\mathrm{d}E_0(p)}{\mathrm{d}p}$$

Assuming a small force, we expand the velocity as $\langle\hat{v}\rangle' = v_0(p) - \mu(p)F$, with the mobility

$$\mu(p) = \frac{1}{eB}\left(1 - M\frac{\mathrm{d}v_0}{\mathrm{d}p}\right)$$

This formula is analogous to the expression for the Hall mobility in our synthetic system. As shown in Extended Data Fig. 3c, it is close to the classical Hall drift in an infinite plane in the bulk mode region $p \gtrsim \hbar/\ell$, while it decreases towards zero in the edge mode region $p<0$.

The overall response of an energy branch in the ground band can be obtained by summing the drifts of all populated eigenstates, such that the centre of mass drift reads

$$\langle v(t)\rangle' = \langle v(t)\rangle_0 - F\int \mathrm{d}p\ n(p)\mu(p)$$

where we assume the normalization $\int \mathrm{d}p\ n(p) = 1$ for the occupation number $n(p)$. We consider a uniform occupation of the lowest energy band, restricted to the energy branch $E_0(p) < \hbar\omega_c$, that is, in the middle of the bulk gap to the first excited band in the bulk. This condition corresponds to momentum states $p > p^* \simeq 0.54\hbar/\ell$ of the ground band. Assuming an upper momentum cutoff p' in the bulk region, we obtain the Hall drift

$$\langle v(t)\rangle' = \langle v(t)\rangle_0 - \frac{F}{eB}\left(1 - M\frac{v_0(p') - v_0(p^*)}{p' - p^*}\right)$$

As long as $p' \gg \hbar/\ell$, the second term can be neglected, and one recovers the Hall drift of a topological band of Chern number $\mathcal{C} = 1$.

We finally consider the local Hall response in the ground band, quantified by the local Chern marker[22]

$$C(x,y) = 2\pi\mathrm{Im}\langle x,y|[\hat{P}\hat{x}\hat{P}, \hat{P}\hat{y}\hat{P}]|x,y\rangle$$

where $\hat{P}$ projects on the considered branch of states and $|x,y\rangle$ are localized in (x, y). The calculation of the Chern marker starts by decomposing position states into momentum states, as

$$C(x,y) = \frac{2}{\hbar}\ \mathrm{Im}\left[\int \mathrm{d}p\ \mathrm{d}q\ \mathrm{e}^{i(p-q)x/\hbar}\phi_p(y)\phi_q^*(y)\tilde{c}(p,q)\right]$$

where $\tilde{c}(p,q) \equiv \langle\psi_p|\hat{x}\hat{P}\hat{y}|\psi_q\rangle$, which can be evaluated using the explicit form of equation (6) for momentum states as

$$\tilde{c}(p,q) = i\hbar\ \langle y\rangle_q\langle\phi_p|\phi_q\rangle\delta'(p-q)$$

where $\langle y\rangle_q$ is the mean y position in the wavefunction ϕ_q. Using the general formula

$$\int \mathrm{d}u\ \mathrm{d}v\ f(u,v)\delta'(u-v) = \int \mathrm{d}u\ \mathrm{d}v\frac{\partial_v f(u,v) - \partial_u f(u,v)}{2}\delta(u-v)$$

we obtain the expression for the Chern marker

$$C(x,y) = \int \mathrm{d}p\ |\phi_p(y)|^2\frac{\mathrm{d}\langle y\rangle_p}{\mathrm{d}p}$$

The relation $p = Mv_0 + qB\langle y\rangle_p$ then leads to

$$C(x,y) = \int \mathrm{d}p\ |\phi_p(y)|^2\mu(p) \qquad (7)$$

a relation analogous to the local Chern marker expression for our synthetic Hall system. We show in Extended Data Fig. 3e the Chern marker calculated for an energy branch $E(p) < \hbar\omega$, which is close to 1 for $y \gtrsim \ell$, and decreases towards zero when approaching the edge $y=0$, similarly to the decrease of the Chern marker close to the edges shown in Fig. 4c.

Local Chern marker in synthetic dimension. In the synthetic Hall system, the expression of the local Chern marker reads

$$C(x,m) = 2\pi\mathrm{Im}\langle x,m|[\hat{P}\hat{x}\hat{P}, \hat{P}\hat{J}_z\hat{P}]|x,m\rangle \qquad (8)$$

Translation invariance along x ensures that the Chern marker only depends on the coordinate m. In the main text, the notation $|m\rangle$ refers to an arbitrary $|x,m\rangle$ state, the choice of x being irrelevant. The derivation of the Chern marker $C(m) = \int \mathrm{d}p\ \Pi_m(p)\mu(p)$ is obtained following the same procedure as for a standard Hall system, discussed above. So far, we have only considered one component μ_{xm} of the mobility tensor—the one that measures the drift along x resulting from a force along m. One can also consider the other component, which quantifies the magnetization drift $\mathrm{d}\langle\hat{J}_z\rangle/\mathrm{d}t$ that results from a force F_x along x. In a linear response, it is defined as $\langle\hat{J}_z\rangle = \langle\hat{J}_z\rangle_0 - \mu_{mx}(p)F_x t$, where μ_{mx} explicitly designates the mobility component considered here, and $\langle\hat{J}_z\rangle_0$ is the unperturbed magnetization. Its expression is given by

$$\mu_{mx} = -\frac{\mathrm{d}}{\mathrm{d}F_x}\frac{\mathrm{d}\langle\hat{J}_z\rangle}{\mathrm{d}t} = -\frac{\mathrm{d}\langle\hat{J}_z\rangle(p)}{\mathrm{d}p}$$

where we used $F_x = \dot{p}$ and the fact that $\langle\hat{J}_z\rangle_0$ is time-independent. The expression $\hat{p} = M\hat{v} + p_{\mathrm{rec}}\hat{J}_z$ allows us to recover the relation $\mu_{mx} = -\mu_{xm}$ between the two transverse mobilities.

We show in Extended Data Fig. 4b,c the measurements of both mobilities as a function of p, and find good agreement between them. We also present in Extended Data Fig. 4d the local Chern markers computed using the data of each mobility.

In the main text, the Chern marker is evaluated over a branch of the ground band, below an energy threshold shown in Extended Data Fig. 4a (at half the cyclotron gap at $p=0$). We also show the Chern marker computed using all momentum states (grey points). Compared to the restricted branch, we only find a discrepancy on the edges of the ribbon. In the region $-5 \leq m \leq 5$, the values are nearly identical, showing that the bulk topological response is insensitive to the momentum cutoff.

We also evaluate theoretically the effect of disorder on the Chern marker. For this, we consider a finite-sized system of length $L = 5\lambda/2$, with periodic boundary conditions along x, and discretized on a grid $(x_n = n\delta x, m)$ of spacing $\delta x = \lambda/40$. The atom dynamics is described by Hamiltonian (2) with an additional disorder potential, taken as a random energy at each site (x_n, m) drawn according to a normal distribution of r.m.s. Δ. We calculate the energy spectrum and the local Chern marker using the equation (8), where $\hat{P}$ projects on the eigenstates of energy $E < E^*$, where $E^* = \hbar\omega_c$ is the middle of the bulk gap. We show in Extended Data Fig. 5a an example of Chern marker distribution in the region $|x_n| < \lambda/2$ for a disorder strength $\Delta = E_{\mathrm{rec}}$. We define a coarse-grained average at the centre of the synthetic dimension as

$$\bar{C}(m=0) = \langle C(x_n, m=0)\rangle_{|x_n| < \lambda/4}$$

We show in Extended Data Fig. 5b the variation of $\bar{C}(m=0)$ with the disorder strength Δ, averaged over 100 disorder realizations for each value of Δ. We find that the central Chern marker is almost unchanged for disorder strengths $\Delta \lesssim 2E_{\mathrm{rec}}$, demonstrating the robustness of the Chern marker in the bulk of the sample.

Abrikosov vortex lattices. The role of interactions in the ground band is assumed to be governed by a single parameter g, which describes contact interactions in both the real and synthetic dimensions (see Supplementary Information). We consider a gas of bosonic atoms with high filling fractions, for which the many-body ground state is well captured by mean-field theory. The system is described by a spinor classical field $(\psi_m(x))$ (with $-J \leq m \leq J$), whose dynamics is governed by the Gross–Pitaevskii equation

$$\begin{aligned} i\hbar\dot{\psi}_m = &\frac{\hbar^2}{2M}(i\partial_x + Km)^2\psi_m - \hbar\Omega\left(\frac{\sqrt{J(J+1) - m(m+1)}}{2}\psi_{m-1}\right. \\ &\left. + \frac{\sqrt{J(J+1) - m(m-1)}}{2}\psi_{m+1} + \frac{m^2}{2J+3}\psi_m\right) + g|\psi_m|^2\psi_m \end{aligned}$$

From the phenomenology of Abrikosov vortex lattices, we expect the ground state to break translational invariance along the real dimension, with an unknown periodicity L_0. To find L_0, we numerically calculate the ground state on a cylinder of circumference L, corresponding to periodic boundary conditions along the real dimension, by evolving the Gross–Pitaevskii equation in imaginary time. We find that the ground-state energy is minimized for a set of circumferences L, integer multiples of a length that we identify as L_0.

The thermodynamic properties are determined by the coupling Ω and the interaction energy scale $g\langle n\rangle$, where $\langle n\rangle$ is the mean atom density, or equivalently by the chemical potential μ_{chem}. Here we explore situations in which the chemical potential lies in the gap between the lowest Landau level and the first excited band (Extended Data Fig. 6b).

For large enough interactions, we always find ground-state configurations in the shape of Abrikosov triangular vortex lattices, such as the ones presented in the main text (Fig. 5). We give in Extended Data Fig. 6a,b another example of such a ground state, represented here by both the density profile and the phase associated to the wavefunction. Around each local minimum of the density, the phase profile is reminiscent of the phase winding of a quantum vortex in a continuous 2D system.

The hard walls in the synthetic dimension have a strong impact on the vortex lattice geometry. We distinguish the different configurations by counting the number of vortex lines along x. For example, in Extended Data Fig. 6a we identify a configuration made of three vortex lines. The phase diagram, shown in Extended Data Fig. 6c, shows a large variety of vortex configurations. Typically, the distance between lines is set by the magnetic length ℓ_{m} in the synthetic dimension. The reduction of the number of vortex lines with Ω is thus explained by the increase of ℓ_{m}. Similarly to type-II superconductors in a confined geometry, the different vortex configurations are separated by first-order transition lines.

The observation of such vortex lattices demands a high-resolution in situ imaging resolved in m space. However, the spontaneous breaking of translational symmetry can be revealed in the momentum distribution—accessible in standard time-of-flight experiments—via the occurrence of Bragg diffraction peaks at multiples of the momentum $p_0 = h/L_0$. As shown in Extended Data Fig. 6d, the expected variation of p_0 with the coupling Ω indirectly reveals the occurrence of phase transitions between different vortex configurations.

Data availability

Source data, as well as other datasets generated and analysed during the current study, are available from the corresponding author upon request. Source data are provided with this paper.

Code availability

The source code for the numerical simulations of the Abrikosov vortex lattices and the Laughlin states are available from the corresponding author upon request. Source data are provided with this paper.

References

44. De Bièvre, S. & Pulé, J. V. Propagating edge states for a magnetic Hamiltonian. *Math. Phys. Electron. J* **2002**, 39–55 (2002).

Acknowledgements

We thank J. Beugnon, N. Cooper, P. Delpace, N. Goldman, L. Mazza and H. Price for stimulating discussions. We acknowledge funding from the EU under ERC projects 'UQUAM' and 'TOPODY', and PSL research university under the project 'MAFAG'.

Author contributions

All authors contributed to the set-up of the experiment, data acquisition, data analysis and the writing of the manuscript.

Competing interests

The authors declare no competing interests.

Additional information

Supplementary information is available for this paper at https://doi.org/10.1038/s41567-020-0942-5.

Correspondence and requests for materials should be addressed to S.N.

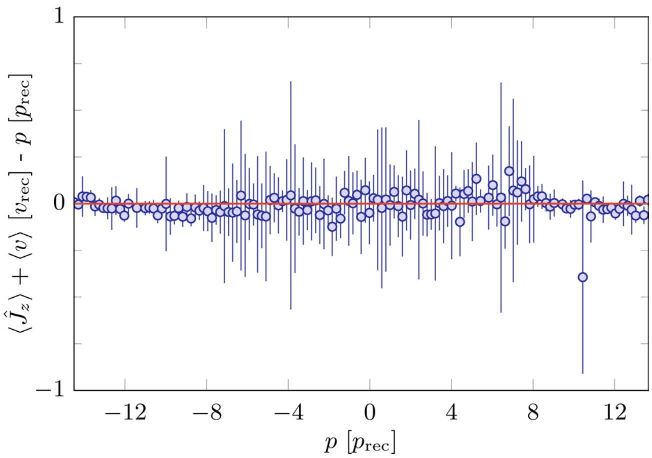

Extended Data Fig. 1 | Conservation of canonical momentum. Difference between the measured canonical momentum $p_{\rm rec}\langle \hat{J}_z \rangle + M\langle \hat{v} \rangle$ and the targeted value p defined by the state preparation protocol. All error bars are the 1-σ standard deviation of typically 5 measurement repetitions.

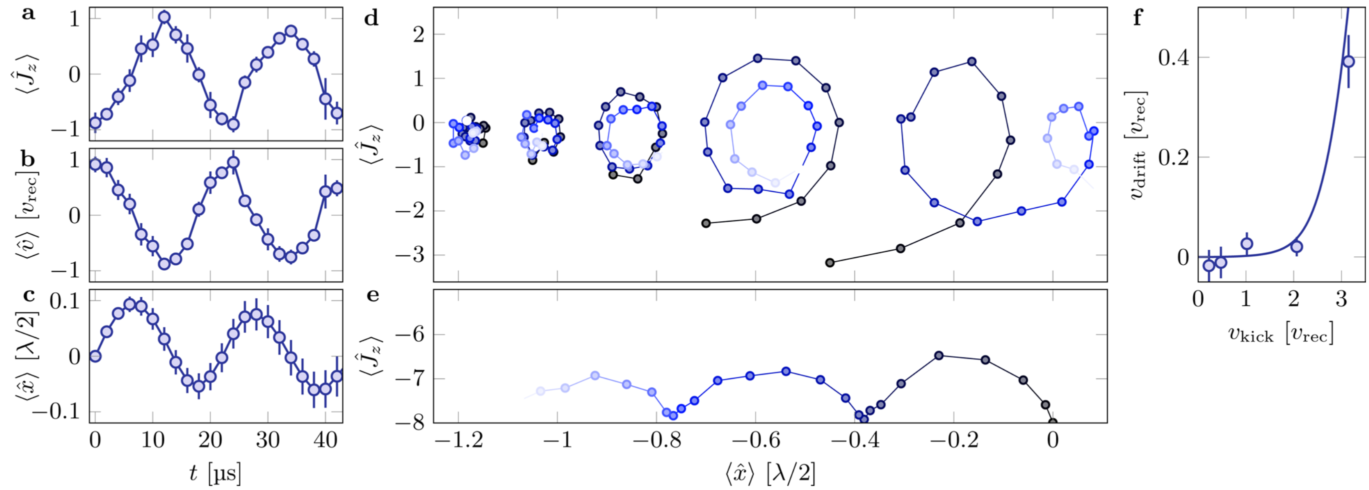

Extended Data Fig. 2 | Cyclotron orbits measurements. **a**, **b**, **c**, Magnetization, velocity and position response as a function of time after application of a velocity kick $v_{\mathrm{kick}} \approx v_{\mathrm{rec}}$. **d**, Bulk excitations corresponding to different velocity kicks, $v = 0.23$, 0.48, 1.02, 2.06, and 3.15 v_{rec}, from left to right. The orbits are off-centred in real space for visual clarity. **e**, Skipping orbit for the momentum state $p = -J\, p_{\mathrm{rec}}$ following a sudden jump of the coupling strength Ω. **f**, Velocity drift of the orbits as a function of the amplitude kick. The solid line corresponds to the expected drift due to the non-harmonic spectrum of the energy bands. All error bars are the 1-σ standard deviation of typically 5 measurement repetitions.

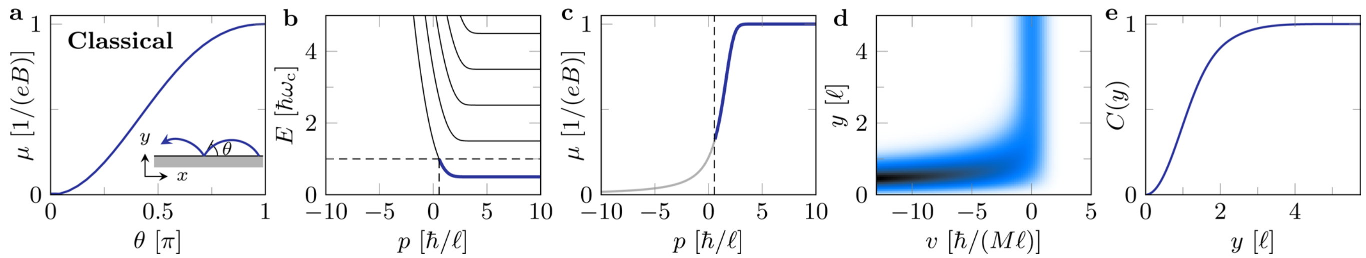

Extended Data Fig. 3 | Hall system in real dimensions. a, Variation of the Hall mobility for classical skipping orbits, depending on the angle of rebound on a hard wall. The case of closed cyclotron orbits corresponds to $\theta = \pi$. **b**, Dispersion relation of a quantum Hall system in a semi-infinite geometry $y > 0$. The blue line indicates the energy branch used for the Chern marker calculation, defined by $E_0(p) < \hbar\omega_c$. **c**, Hall mobility μ as a function of momentum p. **d**, Local density of state in the (v, y) plane. **e**, Local Chern marker $C(y)$ for the energy branch defined in **b**.

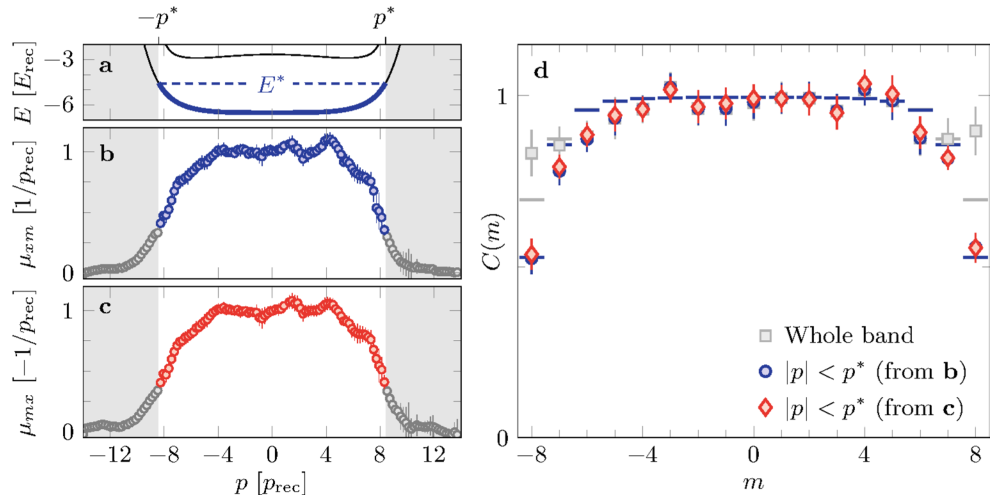

Extended Data Fig. 4 | Hall mobility and local Chern markers. **a**, Predicted dispersion relation for $\hbar\Omega = E_{rec}$. The branch pictured in blue, chosen as $E(p) < E^*$ with E^* at half the gap, is used for the computation of the local Chern marker. **b**, Measured mobility in x resulting from the application of a force along m, as presented in the main text. The points in blue, corresponding to $|p| < p^*$ (white area), are the ones considered for the Chern marker presented in the main text (see Fig. 4). **c**, Measured mobility in m resulting from the application of a force along x. As for **b**, the points in red are associated to momentum states lying below E^*. **d**, Chern marker obtained from the measured mobility, using the whole energy branch ($-\infty < p < \infty$, gray squares, using data in **b**), or using the branch defined in **a** ($-p^* < p < p^*$). For the latter, the blue dots correspond to the data in **b**, and are identical to Fig. 4. The red diamonds correspond to the data in **c**. Solid lines are theoretical values. The error bars are the 1-σ statistical uncertainty calculated from a bootstrap sampling analysis over typically 100 pictures (**b**,**c**) and 1000 pictures (**d**).

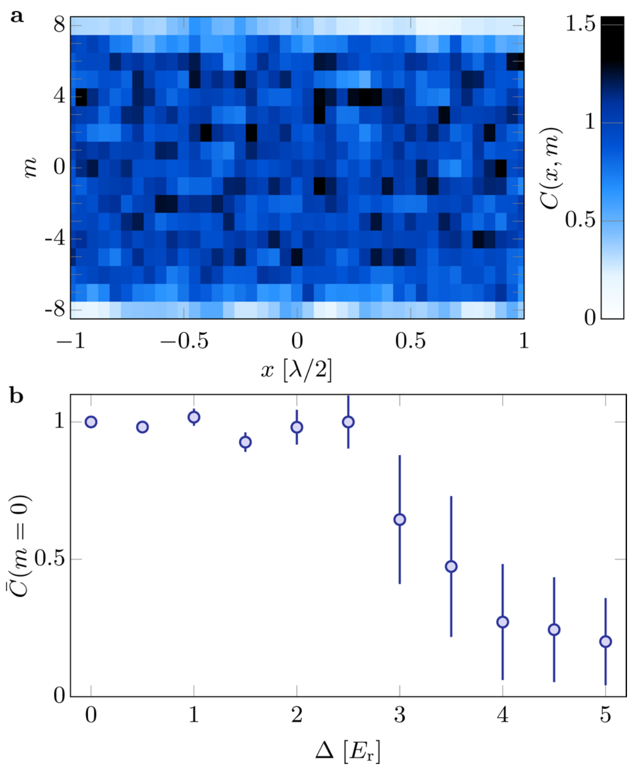

Extended Data Fig. 5 | Effect of disorder. a, Example of Chern marker distribution in the presence of disorder of strength $\Delta = E_{rec}$. **b**, Chern marker $\bar{C}(m = 0)$ averaged over the region $|x| < \lambda/4$ as a function of the disorder strength Δ. Each point is the average of 100 disorder realizations, the error bar showing the standard deviation of the mean.

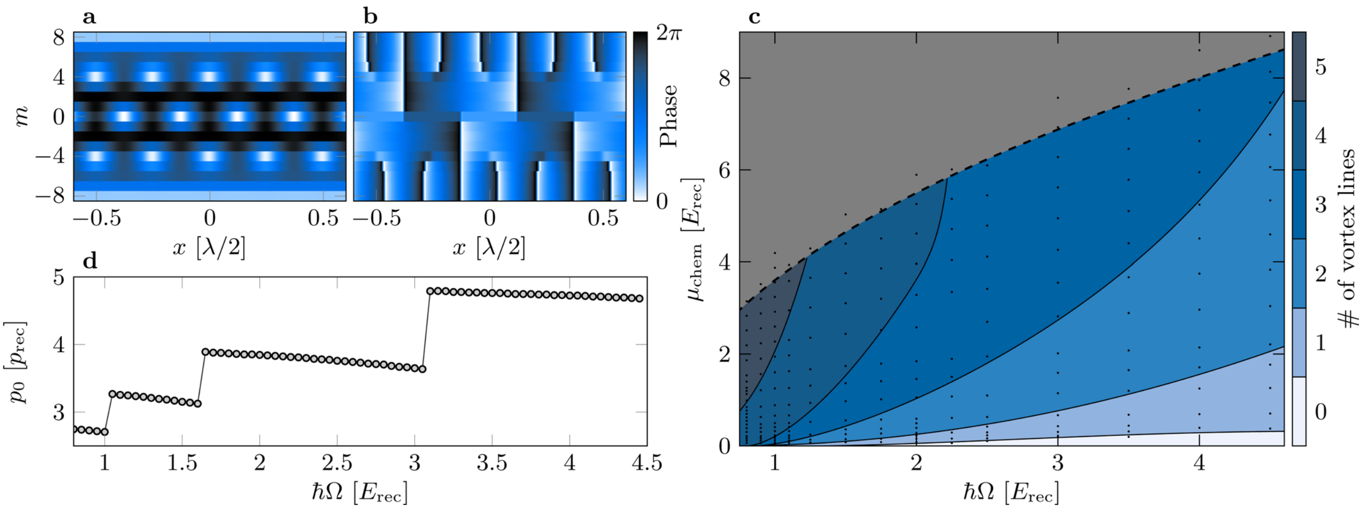

Extended Data Fig. 6 | Abrikosov vortex lattices. a, Ground state density profile and **b**, associated phase, for $\hbar\Omega = 3E_{rec}$ and for $\mu_{chem} \approx 4E_{rec}$. The local minima of the density exhibit a phase winding around them, and thus correspond to quantum vortices. **c**, Number of vortex lines as a function of the Raman coupling Ω and the chemical potential μ_{chem}. The dots identify the configurations for which a simulation was realized. The color encodes the number of vortex lines that characterizes the low-energy vortex lattice configuration. The phase separation lines are guides to the eye. The dashed line identifies the gap to the first excited band above which the atoms significantly occupy higher Landau levels. **d**, Momentum p_0 associated to the spontaneous breaking of the translational invariance resulting from the appearance of a vortex lattice, as a function of Ω. The points were taken at a chemical potential corresponding to half the gap.